



## Spin-states in MoS<sub>2</sub> thin-film transistors distinguished by operando electron spin resonance

Naho Tsunetomo<sup>1</sup>, Shohei Iguchi<sup>1</sup>, Małgorzata Wierzbowska <sup>2</sup>, Akiko Ueda<sup>3,4</sup>, Yousang Won<sup>1</sup>, Sinae Heo<sup>5,6</sup>, Yesul Jeong<sup>5,7</sup>, Yutaka Wakayama<sup>5,6</sup> & Kazuhiro Marumoto <sup>1,8</sup>✉

Transition metal dichalcogenide MoS<sub>2</sub> is a two-dimensional material, attracting much attention for next-generation applications thanks to rich functionalities stemming from its crystal structure. Many experimental and theoretical works have focused on the spin-orbit interaction which couples the valley and spin degrees of freedom so that the spin-states can be electrically controllable. However, the spin-states of charge carriers and atomic vacancies in devices have not been yet elucidated directly from a microscopic viewpoint. Here, we report the spin-states in thin-film transistors using operando electron spin resonance spectroscopy. We have observed clearly different electron spin resonance signals of the conduction electrons and atomic vacancies, and distinguished the corresponding spin-states from the signals and theoretical calculations, evaluating the gate-voltage dependence and the spin-susceptibility and *g*-factor temperature dependence. This analysis gives deep insight into the MoS<sub>2</sub> magnetism and clearly indicates different spin-scattering mechanisms compared to graphene, which will be useful for improvements of the device characteristics and new applications.

<sup>1</sup>Division of Materials Science, University of Tsukuba, Tsukuba, Japan. <sup>2</sup>Institute of High Pressure Physics, Warsaw, Poland. <sup>3</sup>Spintronics Research Center, National Institute of Advanced Industrial Science and Technology (AIST), Tsukuba, Japan. <sup>4</sup>Department of Electrical Engineering, Columbia University, New York, NY, USA. <sup>5</sup>International Center for Materials Nanoarchitectonics (MANA), National Institute for Materials Science (NIMS), Tsukuba, Japan.

<sup>6</sup>Department of Chemistry and Biochemistry, Faculty of Engineering, Kyushu University, Tsukuba, Japan. <sup>7</sup>Busan Center, Korea Basic Science Institute (KBSI), Busan, Republic of Korea. <sup>8</sup>Tsukuba Research Center for Energy Materials Science (TREMS), University of Tsukuba, Tsukuba, Japan.

✉email: [marumoto@ims.tsukuba.ac.jp](mailto:marumoto@ims.tsukuba.ac.jp)

Since graphene was discovered in 2004, two-dimensional (2D) layered materials have attracted much attention. Among them, transition metal dichalcogenides (TMDs) denoted as  $\text{MX}_2$  have been extensively studied. TMDs, with their representative material  $\text{MoS}_2$ , possess desired electrical and optical properties such as high mobility, circular-polarized light emission and flexibility, thus deserving wide investigation also in the field of valleytronics<sup>1–4</sup>. The synthesis of  $\text{MoS}_2$  and their new application have been discussed<sup>5,6</sup>. The bandgap in  $\text{MoS}_2$  single layer is direct, while it becomes indirect with increasing number of layers<sup>7</sup>. Since the nonzero bandgap exists in both the single layer and bulk,  $\text{MoS}_2$  is expected to be applicable in the thin-film devices as a next generation of graphene, the performance of which about the on/off ratio exceeds that with graphene because of a zero bandgap in graphene<sup>3,8–10</sup>. High electric field effect can be applied using ionic liquid, and the electric field-induced superconductivity, electrically switchable chiral light emission, and carrier spin relaxation in electrically doped  $\text{MoS}_2$  have been discussed in transistor structures with the ionic-liquid insulator<sup>11–13</sup>. It has been reported that the aforementioned properties are caused by the conduction- and valence-band splitting by the spin-orbit interaction (SOI)<sup>14–16</sup>, weak electronic localization, and spin-orbit scattering (SOS)<sup>17</sup>, discussed from the theoretical and experimental viewpoints. The spin states of atomic vacancies have been studied using the density functional theory (DFT)<sup>18–20</sup>. Although the spin-states investigation is an important issue for the fundamental understanding of  $\text{MoS}_2$  and applications of its magnetic properties, this matter in device structures under device operation has not been yet fully elucidated experimentally<sup>21</sup>.

Electron spin resonance (ESR) spectroscopy is useful for the spin-states study of the organic electronic devices, such as transistors, solar cells, and light-emitting diodes<sup>22–24</sup>. From the ESR study of graphene transistors, we have found a correlation between atomic vacancies and their conducting mechanisms<sup>25</sup>. That is, spins exist in the charge-neutral graphene due to atomic vacancies; however, when positive or negative gate voltage is applied, spins vanish and then the spin scattering of charge carriers decreases. Thus the electrically induced ambipolar spin

vanishment is believed to contribute to the high carrier mobility in graphene<sup>25</sup>. Previous reports for  $\text{MoS}_2$  materials include the ESR and DFT studies of the atomic vacancies, antisites, impurities, etc. in  $\text{MoS}_2$  crystal and thin films<sup>18–21,26–29</sup>. For  $\text{MoS}_2$  transistors, the theoretical studies, fabrication methods, and device performance characterizations have been conducted<sup>3,4,8,10,11</sup>; however, operando ESR study of  $\text{MoS}_2$  devices has not been yet performed. Elucidation of the spin states of charge carriers and atomic vacancies is important for understanding the physical properties and functioning of  $\text{MoS}_2$  transistors.

Here we report  $\text{MoS}_2$  thin-film transistor spin states using the operando ESR. We have successfully observed several ESR signals, exhibiting various kinds of the electric field response, and identified their origins as derived from the conduction electrons or atomic vacancies. The ESR signal changes under the applied gate voltage are compared with the  $g$ -factor variation calculated with the gauge-including projector-augmented wave (GIPAW) method<sup>30</sup>. The temperature dependence of measured  $g$ -factors reflects the SOI and SOS and is compared to the theoretical results using the Mori-Kawasaki formula<sup>31</sup>. Therefore, these studies give an important information on the microscopic properties of  $\text{MoS}_2$  in the transistor structures. Compared to the previous ESR studies of  $\text{MoS}_2$  materials, the novel contribution of the present work is the spin-state investigation in  $\text{MoS}_2$  device structures under device operation.

## Results

**Device fabrication and characterization.** In this work, we used a device configuration called the side-gate structure, schematically presented in Fig. 1a with its cross-section in Fig. 1b. The  $\text{MoS}_2$  thin film was formed on the sapphire ( $\text{Al}_2\text{O}_3$ ) substrate with a multi-step chemical vapor deposition (CVD) method<sup>32,33</sup>. The gate, source, and drain electrodes of Ni/Au (1/49 nm) were fabricated on  $\text{Al}_2\text{O}_3$  or  $\text{MoS}_2$  with a vacuum deposition method. The insulating layer of the transistor structure was formed by the ion-gel electric double layers (EDLs), which enable to obtain a higher charge density at the low gate voltages than that of the

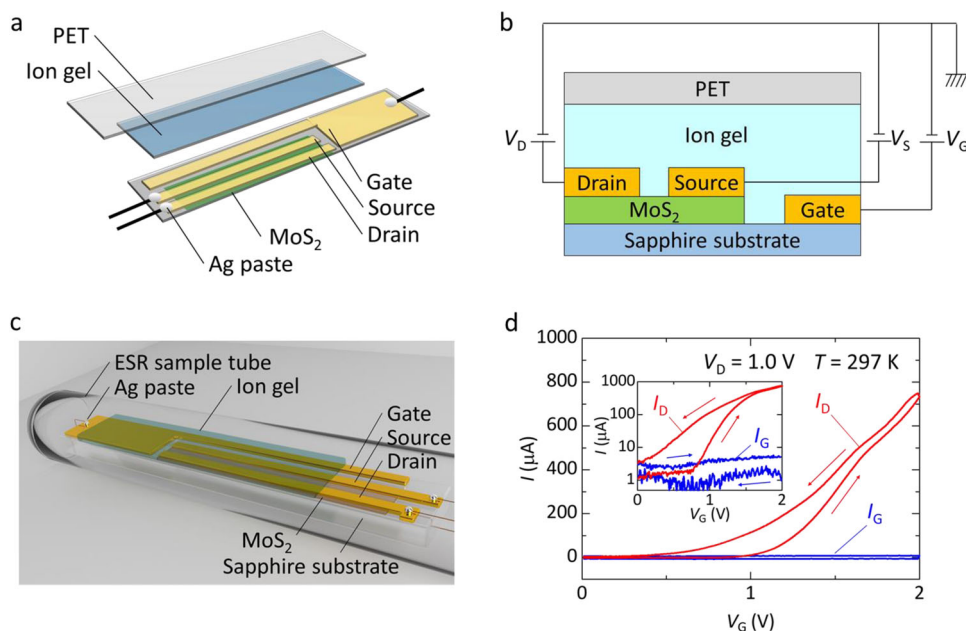


**Fig. 1**  $\text{MoS}_2$  transistor structure and device characteristics. **a** Schematic diagram of the device structure of a  $\text{MoS}_2$  transistor used for ESR measurements. **b** Schematic cross-section of the device structure. **c** Schematic diagram of the  $\text{MoS}_2$  transistor in an ESR sample tube. **d** Transfer characteristic of the  $\text{MoS}_2$  transistor. The inset shows a plot of the transfer characteristics in logarithmic scale.

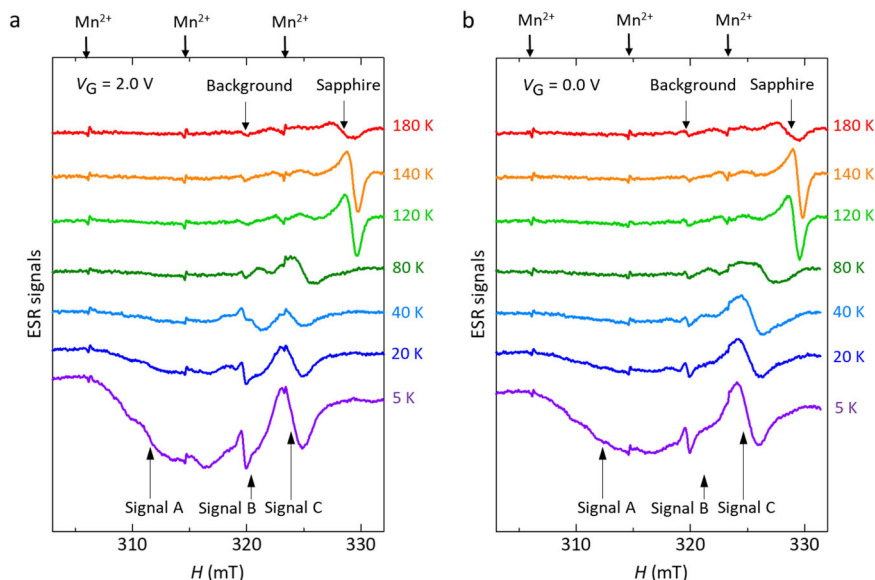


**Fig. 2 Temperature and gate-voltage dependence of ESR spectra of the MoS<sub>2</sub> transistor.** **a** ESR spectra measured at a gate voltage ( $V_G$ ) of  $V_G = 2$  V and a drain voltage ( $V_D$ ) of  $V_D = 1$  V. **b** ESR spectra measured at  $V_G = 0$  V and  $V_D = 1$  V. Distortion of the baseline of the spectra at low temperatures, typically below 40 K, is due to the background signal of the ESR cavity resonator.

conventional solid insulating layers<sup>34</sup>. The ion gel was formed on the polyethylene terephthalate (PET) substrate by drop casting and thermally annealed under the vacuum conditions. Then the whole system was annealed and laminated in the N<sub>2</sub>-filled glove box and wired using the Ag paste. The fabricated transistor was inserted into the ESR sample tube and sealed under He atmosphere, as presented in Fig. 1c. Details of the device fabrication method are described in the “Methods” section.

The spin states in the device were observed with the operando ESR spectroscopy using the liquid-He cryostat, which enables to perform measurements from 4 K to room temperature. The direction of the external magnetic field ( $H$ ) was perpendicular to the MoS<sub>2</sub> film plane unless otherwise stated. The gate voltage ( $V_G$ ) and drain voltage ( $V_D$ ) were controlled by an analyzer or a source meter, such that the operando ESR signals were measured simultaneously with the drain current ( $I_D$ ) and gate current ( $I_G$ ). Figure 1d shows the typical transfer characteristics of the fabricated device. The  $I_D$  increased with the  $V_G$  being positive and the n-type behavior was confirmed. The field-effect mobility  $\mu = 6.6$  cm<sup>2</sup> V<sup>-1</sup> s<sup>-1</sup> and on/off ratio of 436 were obtained as the transistor parameters. The evaluated mobility and on/off ratio are lower than those of >100 cm<sup>2</sup> V<sup>-1</sup> s<sup>-1</sup> and >10<sup>4</sup> reported in the previous works<sup>3,11</sup>. The reason may be ascribed to much longer channel length (500  $\mu$ m) of our transistor than that (<15  $\mu$ m) of the previous works because the mobility and on/off ratio are strongly affected by the charge transport across the grain boundaries of the MoS<sub>2</sub> film in the transistor channel<sup>3,11</sup>. Another reason for the low mobility and on/off ratio may be attributed to the defectivity in the MoS<sub>2</sub> film, as discussed later. The low mobility and on/off ratio, however, do not affect the ESR measurements because the ESR method does not require such charge transport. The reason of the use of such long channel length in the transistor structure is that we need a large active area of the transistor channel to improve the signal-to-noise ratio of the electrically induced ESR signal. The inset of Fig. 1d shows the transfer characteristics in logarithmic scale. The transistor in the forward scan is fully off at  $V_G = 0$  V. However, the transistor in the backward scan is not fully off at  $V_G = 0$  V, which may be ascribed to the slow relaxation of electric double layers due to

ionic liquid in the ion gel in the side-gate transistor structure. “Methods” section contains more details of the characterization.

**Operando spin observation of conduction electrons and atomic vacancies.** Typical measured ESR spectra at  $V_G = 2$  and 0 V are presented in Fig. 2, where three kinds of signals: A, B, and C, are defined from the lowest applied magnetic field. We have measured the ESR spectra in the forward scan. That is, we have first measured the data at  $V_G = 0$  V, in other words, without the  $V_G$  application, and then have measured the data at  $V_G = 2$  V. As shown in the inset of Fig. 1d, the transistor was in the off state at  $V_G = 0$  V in the forward scan. Thus the ESR spectra at  $V_G = 0$  V can be regarded as the background or reference data for the data at  $V_G = 2$  V. Other ESR spectra measured between  $V_G = 2$  and 0 V are similar to that at  $V_G = 2$  V except for electrically induced peak-to-peak ESR intensity, as discussed later. The signals with the opposite phase at around 306, 314, and 323 mT are due to a standard Mn<sup>2+</sup> marker sample. We have confirmed that the signals at around 319 and 329 mT are attributed to the background signal of the ESR cavity resonator and the sapphire substrate, respectively.

The spin states are clearly reflected in the ESR signals and vary due to the electron accumulation under applied  $V_G$ , in “on” and “off” states. In addition, it is considered that the signals derived from the conduction electrons and atomic vacancies will exhibit different temperature dependencies. The former signals are expected to show the Pauli paramagnetism and the latter to obey the Curie law. Figure 2 shows a change of the signal intensity with  $V_G$ . To analyze this effect in detail, we compared the ESR spectra with  $V_G$  switched on and off and obtained the difference spectra shown in Fig. 3b, d, f. Figure 3a, c, e present the  $V_G$  dependence of the ESR spectrum of Signal A, B, and C at a constant temperature, respectively, where the red and blue lines show the spectra at  $V_G = 2$  and 0 V, respectively. The data at  $V_G = 2$  and 0 V contain the background signal and baseline’s distortion due to the ESR cavity resonator. Figure 3b, d, f show the difference spectra of the Signals A, B, and C obtained by subtracting the signals at  $V_G = 0$  V from those at  $V_G = 2$  V. Since Signal A obtained at low temperatures overlapped with the

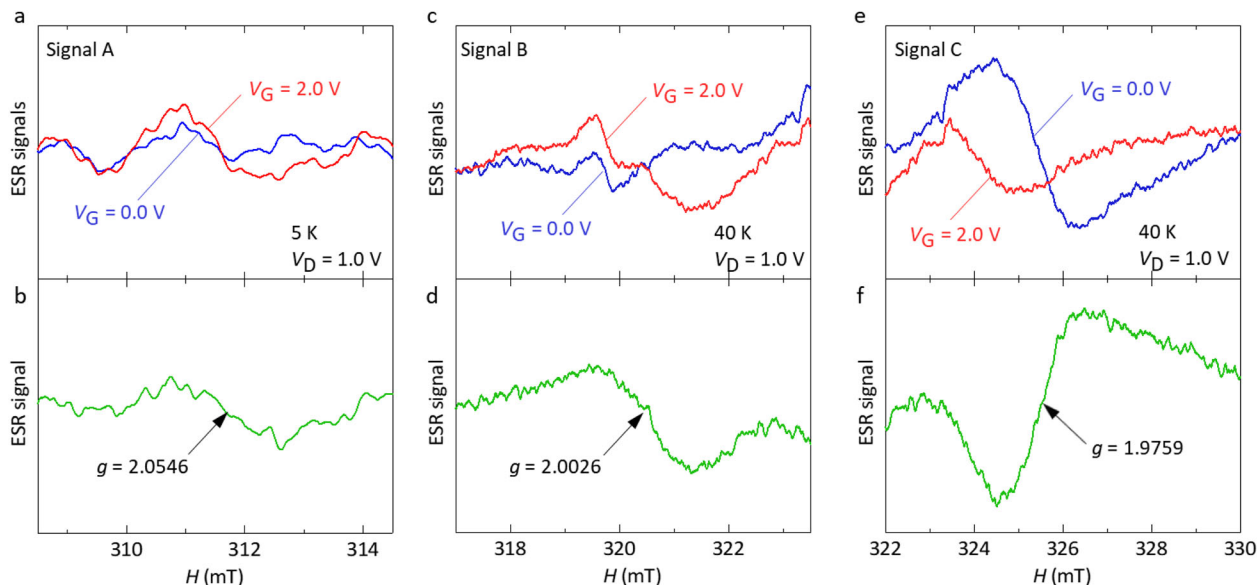


**Fig. 3** Gate-voltage dependence of ESR spectra (upper data) and their difference spectra (lower data). The red lines show the spectra at  $V_G = 2$  V and  $V_D = 1$  V. The blue lines show the spectra at  $V_G = 0$  V and  $V_D = 1$  V. The data at  $V_G = 2$  and 0 V contain the background signal and baseline's distortion due to the ESR cavity resonator. The green lines show the difference spectra obtained by subtracting the ESR spectra at  $V_G = 0$  V from that at  $V_G = 2$  V. These data almost do not contain the background signal and baseline's distortion due to the ESR cavity resonator. **a** Enlarged view of the ESR spectra of Signal A at 5 K shown in Fig. 2. Baseline correction has been performed on the background signal from the ESR cavity resonator. **b** Difference ESR spectrum of Signal A shown in **a**. **c**, **e** Enlarged views of the ESR spectra of the Signals B and C shown in Fig. 2, respectively. **d**, **f** Difference ESR spectrum of the Signals B and C shown in **c**, **e**, respectively.

background signal of the cavity resonator, we evaluated each difference after correcting the corresponding baseline signal. The intensity of Signal A increased with  $V_G$ , and the difference spectrum with  $g$ -factor of  $2.0546 \pm 0.004$  was observed at 5 K. The Signal B also increased with  $V_G$ , and the difference spectrum with  $g = 2.0026 \pm 0.004$  was obtained at 40 K. In contrast, the Signal C with  $g = 1.9759 \pm 0.004$  was observed with  $V_G = 0$  V and its intensity decreased with  $V_G$ ; the decrease is demonstrated by the opposite phase of the difference spectrum as shown in Fig. 3f. The signal intensity and the signal position with respect to the external magnetic field have been calibrated by those of a  $\text{Mn}^{2+}$  marker standard sample. Therefore, it is demonstrated that these signals have different origins, because they show different  $g$ -factor and  $V_G$  dependence. We have confirmed that the  $g$ -factor and ESR linewidth of the difference spectra do not depend on the  $V_G$  for the region of  $0 \text{ V} < V_G \leq 2 \text{ V}$ . Only the peak-to-peak ESR intensity monotonically depends on the  $V_G$ , although the signal-to-noise ratio of the difference spectra is not so good for  $V_G < 2 \text{ V}$ . We do not discuss the  $V_G$  dependence of the ESR intensity in this work in detail. Thus, for clear presentation of the difference spectra, we present the data at  $V_G = 2$  and 0 V as shown in Fig. 3.

Further insight into the spin states such as degenerated conduction electrons or isolated spins and the SOI in  $\text{MoS}_2$  is drawn from the temperature dependence of the spin susceptibility ( $\chi$ ) and  $g$ -factor, respectively, evaluated from the difference spectra (Fig. 3b, d, f) obtained from the ESR spectra at  $V_G = 2$  and 0 V (Fig. 3a, c, e), which are presented in Fig. 4. The SOI determining the  $g$ -factor reflects whether the spin species are due to electrically induced charge carriers or localized charges in electrical devices. Specifically, the temperature dependence of  $\chi$  is presented in Fig. 4a, c, e and of the  $g$  values in Fig. 4b, d, f for the Signals A, B, and C, respectively. The absolute value of  $\chi$  for the Signals A, B, and C has been evaluated by doubly integrating the difference spectrum and comparing it with a  $\text{Mn}^{2+}$  marker sample with  $5.6 \times 10^{11}$  spins, respectively; the marker is attached to the inside wall of the ESR cavity resonator of the ESR system.

Following, we derive the origins of the signals from the features of the  $g$ -factor and  $\chi$ .

### Spin state of conduction electrons and theoretical calculation.

We start with Signal A.  $\chi$  shows almost no temperature dependence, as in Fig. 4a, and this behavior is clearly different from that of the Curie law (dotted line in Fig. 4a), which describes the isolated spins. Therefore, this signal is ascribed to be derived from the degenerated conduction electrons because no temperature dependence of the  $\chi$  indicates Pauli paramagnetism that is derived from the degenerated electron systems. Moreover, the  $g$ -factor generally determined by the SOI decreased with temperature as in Fig. 4b. The  $g$ -factor shift by the intrinsic SOI has been calculated using the DFT method and the value at the zero temperature in the absence of SOS has been reported to be  $g^* \sim 2.21$  (refs. 35,36), which is larger than our experimental result ( $g \sim 2.055$ ). This may imply that some spin states are isolated at atomic vacancies, while the majority of the spins may be located at the conduction band since the  $g$ -factors observed for the isolated spins are smaller than  $g \sim 2$ , as discussed below. Since it has been reported that the spin-relaxation rate rises with increasing temperature<sup>17</sup>, the  $g$ -factor shift may originate from the SOS. In Supplementary Methods, Supplementary Table 1, and Supplementary Fig. 1, we theoretically considered a simple model of the monolayer  $\text{MoS}_2$ , including the SOS and electron-phonon (e-ph) scattering, and assumed that the mechanism of the SOS was the Elliot-Yaffet type (EY) and D'yakonov-Perel' (DP) type, existing in the presence of the magnetic field<sup>37</sup>. The SOS causes the spin relaxation induced by the SOI. This relaxation affects the spin states of conduction electrons, which change the characteristics of spintronic, valleytronic, and optoelectronic devices. The  $g$ -factor shift was derived from the calculation of the ESR response using the Mori-Kawasaki formula<sup>31,38</sup>. In Supplementary Fig. 1, we present a fit of the data in Fig. 4b to the aforementioned model, using the parameters for the SOS and e-ph scattering rate given in

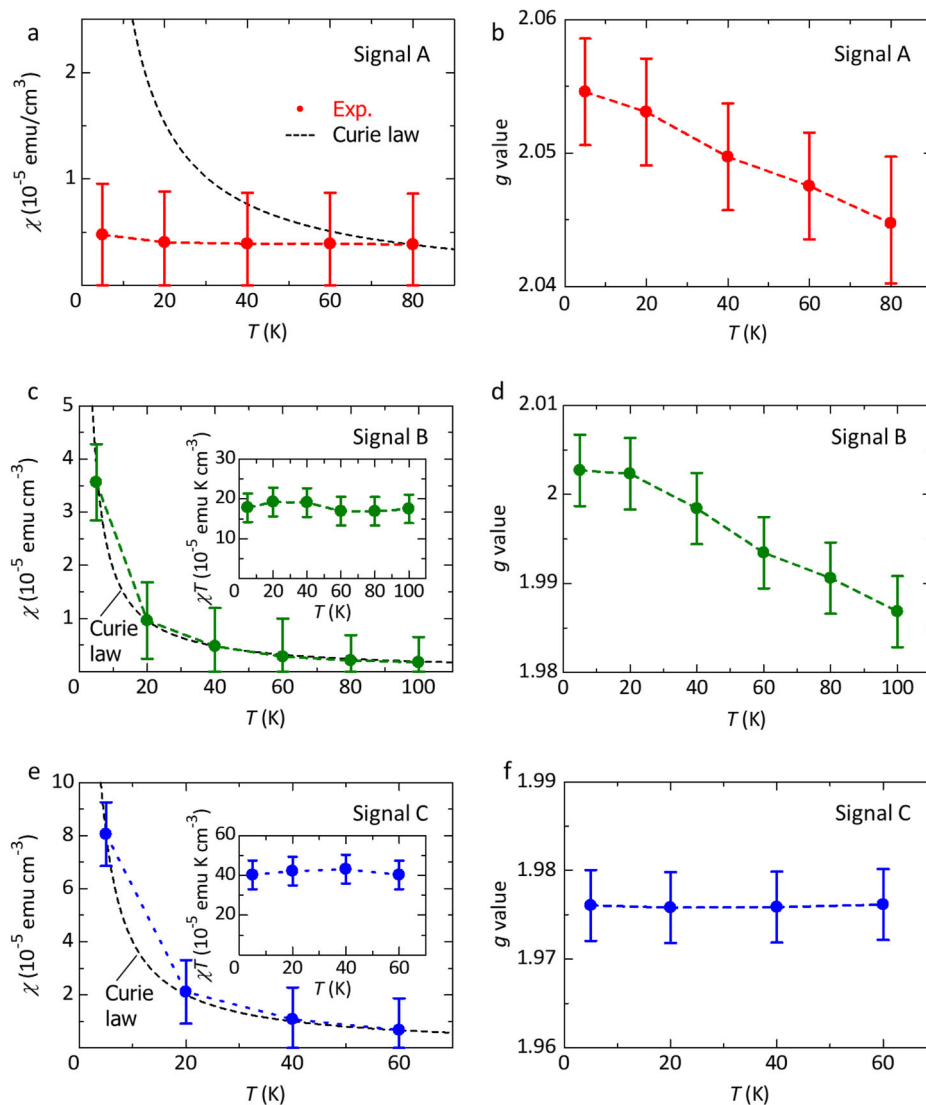


**Fig. 4** Temperature dependence of spin susceptibility and g-factor. **a, c, e** Temperature dependence of the spin susceptibility ( $\chi$ ) of the Signals A, B, and C, respectively. In **c, e**, the plot of  $\chi T$ - $T$  of the Signals B and C is shown, respectively. **b, d, f** Temperature dependence of the g-factor of Signals A, B, and C, respectively. The error bars in **a, c, e** and in **b, d, f** represent the errors from the double integral and baseline's distortion of the difference ESR spectra shown in Fig. 3b, d, f, respectively.

Supplementary Table 1. The result clearly shows that the SOS assisted by the e-ph interaction lowers the g-factor.

To further study the effect of the SOS, we have measured the temperature dependence of the peak-to-peak ESR linewidth  $\Delta H_{pp}$  of the difference spectrum of Signal A. As a result, a decrease of the  $\Delta H_{pp}$  from 1.9 mT at 5 K to 1.8 mT at 60 K has been observed (not shown). This result can be explained by the dominant DP spin relaxation compared to the EY spin relaxation at high temperatures because the DP spin relaxation narrows the ESR linewidth while the EY spin relaxation broadens the linewidth at high temperatures. This dominant DP spin relaxation compared to the EY spin relaxation is supported by the present theoretical calculation. That is, the calculated spin-relaxation time due to the DP type (approximately  $4 \times 10^{-7}$  s at 5 K and  $8 \times 10^{-7}$  s at 100 K) is shorter than that of the EY type (approximately 1 s at 5 K and 0.09 s at 100 K), and thus the DP spin relaxation dominantly determines the ESR linewidth because the linewidth is inversely proportional to the relaxation time.

We observed that the ESR signal lead to the different g-factor when the direction of the external magnetic field ( $H$ ) was changed

from the perpendicular to parallel with respect to the substrate plane. That is, the g-factor angular dependence with respect to the  $H$  direction was observed. When the angle between the  $H$  direction and the normal of the substrate plane increased from  $0^\circ$  (perpendicular) to  $90^\circ$  (parallel), the g-factor monotonically decreased from  $2.0546 \pm 0.004$  to  $1.9836 \pm 0.004$ . Since the orbital angular momentum is different for two orientations of  $H$ , the g-factor measured in the system is confirmed to be determined by the SOI.

**Spin states of different atomic vacancies.** For Signal B,  $\chi$  exhibits the decreasing temperature dependence, as shown in Fig. 4c. The inset of Fig. 4c shows the plot of  $\chi T$ - $T$  of Signal B, which shows an almost constant behavior with respect to the temperature variation. This behavior is characteristic for the Curie law for the isolated spins (see dotted line in Fig. 4c), thus the signal is attributed to the atomic vacancies in the MoS<sub>2</sub> thin films. As shown in Fig. 4d, the g-factor also decreased with temperature. In addition, the  $\Delta H_{pp}$  was obtained as 2.5 mT at 20 K and decreased monotonically to 0.8 mT at 60 K (not shown). Decreasing ESR

linewidth with temperature indicates that the isolated spins are mobile, that is, the motional narrowing of the ESR linewidth. In this case, the SOS effect is believed to increase with temperature. Thus the SOS may contribute to the  $g$ -factor and lowers it with temperature, the same way as for Signal A.

For Signal C, akin to Signal B, a Curie law temperature dependence was observed, in which  $\chi$  decreased with temperature, as shown in Fig. 4e (see dotted line in Fig. 4e).  $\chi$  has been obtained from the ESR spectra at  $V_G = 0$  V because the difference ESR spectrum shows the opposite phase due to the decrease in the ESR intensity by the  $V_G$  application (see Fig. 3f). The inset of Fig. 4e shows the plot of  $\chi T - T$  of Signal C, which shows an almost constant behavior with respect to the temperature variation, as observed for Signal B. Therefore, we ascribe this ESR signal to the isolated spins at atomic vacancies in the  $\text{MoS}_2$  films. No temperature dependence of the  $g$ -factor was observed, as shown in Fig. 4f. In addition,  $\Delta H_{pp}$  did not largely vary, changing from 1.7 to 2.0 mT in the range of 5–60 K (not shown). Therefore, the isolated spins are immobile (or localized), and the effect of the SOS may be small.

**Identifications of atomic vacancies' origins by DFT analysis.** In order to investigate the atomic vacancy states in  $\text{MoS}_2$  in detail, being in the origin of Signals B and C, the DFT calculations were performed. Earlier works report several types of atomic vacancies, and among them, S,  $\text{S}_2$ ,  $\text{MoS}_3$ , and  $\text{MoS}_6$  vacancies have been discussed as the defects that easily occur in  $\text{MoS}_2$  (refs. 18,19,39). Thus we focus on these four types of atomic vacancies. Supplementary Fig. 2 displays examples of calculated spin-density distribution around the above vacancies in the  $\text{MoS}_2$  monolayer, obtained with the DFT method, using the Quantum ESPRESSO package. To mimic the  $n$ -type operation of the ESR, in Supplementary Fig. 2, the spin densities correspond to the negatively charge-doped systems. We introduce the defects and electron doping to a monolayer (mL), bilayer (bL), trilayer (tL), and bulk material. For the bL, three configurations: A, B, and C, of the vacancy localization were considered, as shown in Supplementary Fig. 3. The electron-doping dependence of the magnetization was calculated for the mL, bL, tL, and bulk  $\text{MoS}_2$  without and with the vacancies, and it is presented in Supplementary Fig. 4. As shown in Supplementary Fig. 4, the  $\text{MoS}_2$  films with no vacancy or with S or  $\text{S}_2$  or  $\text{MoS}_3$  vacancy show no magnetization without electron doping (see Supplementary Fig. 4a–c). In contrast, the  $\text{MoS}_2$  films with  $\text{MoS}_6$  vacancy show the magnetization without electron doping (see Supplementary Fig. 4c). These results are useful for identifying the spin species of the observed ESR signals, as discussed later in detail. More detailed spin-density distribution maps are plotted in Supplementary Figs. 5–9. For the charge neutral defects, the local magnetization is non-vanishing only for the  $\text{MoS}_6$  vacancy. That is, the  $\text{MoS}_6$  vacancy in  $\text{MoS}_2$  has the diverse spin densities for spin up and spin down around the vacancy, and thus it has magnetization without electron doping (a non-vanishing state of spin), in other words, the electronic densities with spin up and spin down are different from each other (see Supplementary Figs. 2d, 4c, and 9), while other atomic vacancies in  $\text{MoS}_2$  in addition to pure  $\text{MoS}_2$  layers with no vacancy have equal spin densities for the spin up and spin down, and thus they have no magnetization without electron doping (a vanishing state of spin), in other words, the electronic densities with spin up and spin down are equal to each other (see Supplementary Fig. 4). This result has confirmed that the origin of Signal C is ascribed to the  $\text{MoS}_6$  vacancy, as discussed later. Under the electron doping, the spin density and magnetization decrease for the  $\text{MoS}_6$  vacancy (see Supplementary Figs. 2d, 4c, and 9). In contrast, for the remaining vacancies: S,  $\text{S}_2$ , and  $\text{MoS}_3$ ,

as well as the absence of the defects, the spin density and magnetization increase with weak electron doping (see Supplementary Figs. 2, 4, and 5–8).

As mentioned above, for the charge-neutral film, the calculated spin polarization vanishes for the cases of the S,  $\text{S}_2$ , and  $\text{MoS}_3$  vacancies and no vacancy. This result agrees with the calculated electronic structures with non-vanishing bandgaps (Fig. 5a–d). In contrast, for the  $\text{MoS}_6$  vacancy, the bandgap disappeared for the spin down, indicating a semimetal state (as shown in Fig. 5e, f), which corresponds to the existence of magnetization even for the charge-neutral film.

We compare the experimental and calculated results. As can be seen from Fig. 3e, f, Signal C can be observed even without applied  $V_G$ , and the signal intensity decreases with  $V_G$ . From the DFT results shown in Supplementary Fig. 4c, only the  $\text{MoS}_6$  vacancy state is magnetic without electron doping among the vacancies that have been thought to occur easily in  $\text{MoS}_2$ . Therefore, Signal C is reasonably ascribed to be derived from the  $\text{MoS}_6$  vacancy.

Contrary to Signal C, the intensity of Signal B increases with  $V_G$  (see Fig. 3c, d). Since the magnetization increases with  $V_G$ , three kinds of atomic vacancies: S,  $\text{S}_2$ , and  $\text{MoS}_3$  can be a plausible origin of Signal B, examining the DFT results in Supplementary Fig. 4. To further identify the origin of this signal, the  $g$ -factors corresponding to these three vacancies were calculated, and the results are summarized in Fig. 6. Also, the  $g$ -factor shifts, with respect to the free-electron's value (2.0023) in ppm units, and their dependence on the electron doping are shown in Supplementary Fig. 10. As shown in Fig. 6, the experimental  $g$ -factors of Signal B, of 1.987–2.003, agree with the corresponding numbers obtained from the GIPAW method for the S-vacancy case. Moreover, the  $g$ -factors calculated for the  $\text{S}_2$  and  $\text{MoS}_3$  vacancies do not coincide with the experimental values. Therefore, Signal B could be ascribed as associated with the S vacancy. The S vacancies are commonly observed using some techniques such as transmission electron microscope (TEM). In our study, we have assigned the origin of Signal B from the coincidence of not only the  $g$ -factor but also of the electron-doping dependence of the magnetization by ESR and DFT. That is, Signal B can be first observed with electrically induced electrons without the lattice distortion due to chemical doping. The previous ESR works have mainly studied films without electrically induced electrons without device structures, which may be the reason why the S vacancies have never been reliably observed in ESR.

Recent ESR study of  $\text{MoS}_2$  films grown by metal organic vapor deposition and subsequently transferred on  $\text{SiO}_2/\text{Si}$  has discussed the evidence of a process-induced Mo-vacancy ( $V_{\text{Mo}}$ )-related defect located at  $\text{MoS}_2$  grain edges or boundaries, which has reported the experimental  $g$ -factor of 1.9998 (ref. 40). The previous DFT study of point defects in  $\text{MoS}_2$  has reported the calculated  $g$ -values of S and Mo vacancies ( $V_{\text{S}}$  and  $V_{\text{Mo}}$ ) and antisites ( $\text{S}_{\text{Mo}}$  and  $\text{Mo}_{\text{S}}$ ) as 2.031 for  $V_{\text{S}}$ , 1.994 for  $V_{\text{Mo}}$ , 2.004 for  $\text{S}_{\text{Mo}}$ , and 2.065 for  $\text{Mo}_{\text{S}}$ , respectively<sup>20</sup>. The  $g$ -factor of the experimental and calculated values (1.9998 and 1.994) of the  $V_{\text{Mo}}$  are close to that of Signal C ( $g = 1.9759$ ) under the non-doping state compared to those of other point defects. However, energy-dispersive X-ray spectroscopy (EDX) mapping of the  $\text{MoS}_2$  film used in our study shows that the atomic percentage of sulfur is smaller than the stoichiometric ratio of 2:1 for S:Mo in  $\text{MoS}_2$  (see Supplementary Table 2), which confirms the lack of sulfur in our films. Thus the  $V_{\text{Mo}}$  may be possibly excluded from the origin of Signal C of the  $\text{MoS}_2$  film fabricated by our multi-step CVD method. The amount of substitutional impurities is <1% per the  $\text{MoS}_2$  unit cell as confirmed by EDX mapping of the  $\text{MoS}_2$  film (see Supplementary Fig. 11), and thus substitutional impurities are excluded from the origins of the observed ESR signals because

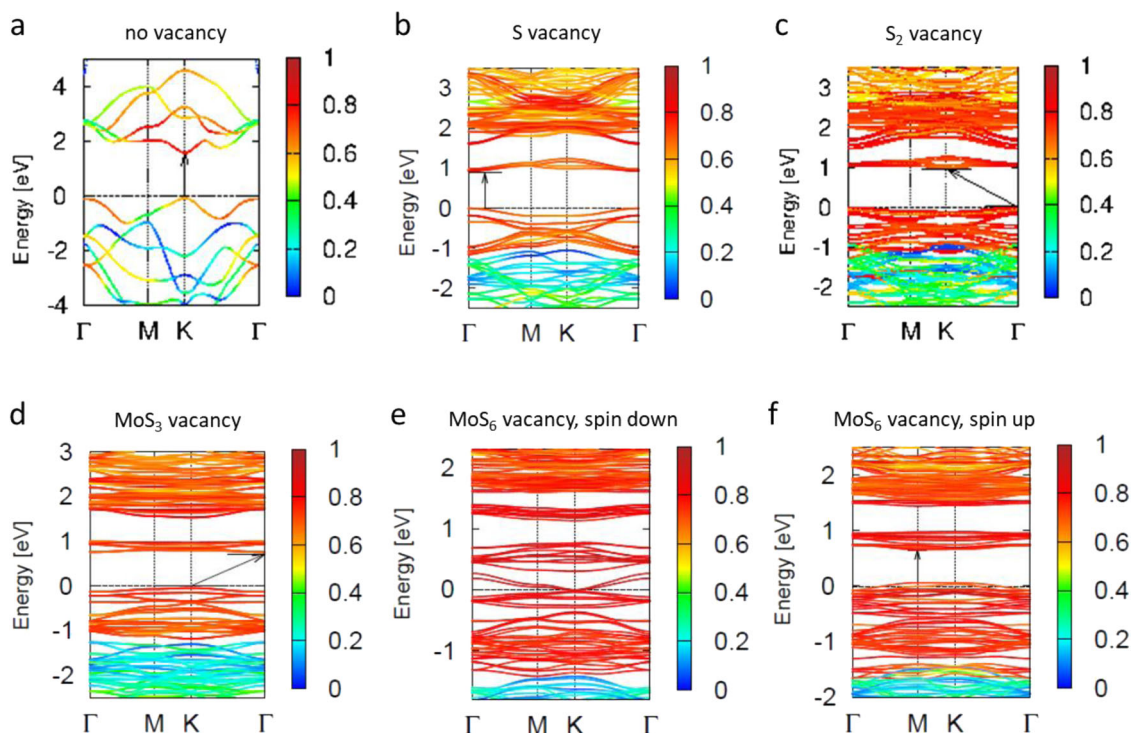


**Fig. 5** Calculated band structures of *mL* MoS<sub>2</sub> without and with various atomic vacancies under no charge injection. **a** MoS<sub>2</sub> with no vacancy. **b** MoS<sub>2</sub> with the S vacancy. **c** MoS<sub>2</sub> with the S<sub>2</sub> vacancy. **d** MoS<sub>2</sub> with the MoS<sub>3</sub> vacancy. **e, f** MoS<sub>2</sub> with the MoS<sub>6</sub> vacancy for **e** spin-down and **f** spin-up case, respectively. When the electron doping is zero, no spin density or no magnetization is calculated for the cases of S, S<sub>2</sub>, and MoS<sub>3</sub> vacancies, as shown in Supplementary Fig. 4. These results are further confirmed by the existence of the bandgap at the Fermi level with no spin density as shown in **b-d**. For the MoS<sub>6</sub> vacancy, the bandgap is closed at the Fermi level depending on the spin direction as shown in **e, f**, which means a semimetal state. The color legend represents the projections of the bands on the Wannier functions localized at the Mo atoms.

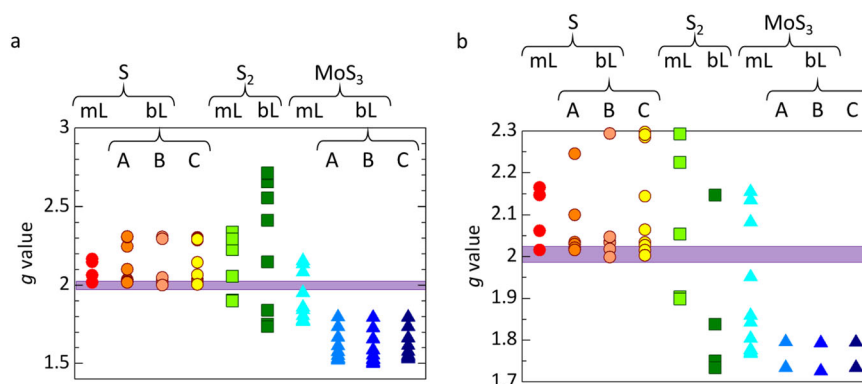


**Fig. 6** Calculated *g*-factor for various atomic vacancies and charge doping. The *g*-factor calculated for the S, S<sub>2</sub>, and MoS<sub>3</sub> vacancies in the MoS<sub>2</sub> supercell of size 12 × 12 × 1 unit, with 1–12 injected electrons, are collectively displayed. Purple area indicates the range of the observed *g*-factors of Signal B (*g* = 1.987–2.003). For the case of bilayer (bL), types A, B, and C are defined depending on the arrangement of atomic vacancies (see Supplementary Fig. 3). These *g*-factors are calculated for the direction of external magnetic field perpendicular to the MoS<sub>2</sub> plane (*z*-axis) (see Supplementary Fig. 10). **a** All calculated *g*-factors for Signal B. **b** Enlarged view near the observed *g*-factors of Signal B (*g* = 1.987–2.003).

the observed spin concentration per the MoS<sub>2</sub> unit cell is >2% (see “Evaluation of spin concentration” in “Methods”).

## Discussion

Our results for the MoS<sub>2</sub> thin films are compared with the previous ones for graphene. The mobility  $\mu$  in graphene has been reported as about tens of thousands cm<sup>2</sup> V<sup>-1</sup> s<sup>-1</sup> (ref. 41), to be compared with values of several hundred to a thousand cm<sup>2</sup> V<sup>-1</sup> s<sup>-1</sup> for MoS<sub>2</sub> (ref. 42). Since carbon atoms of graphene have four valence electrons and three C–C bonds due to the

C3 symmetry, the carbon vacancy necessarily has one unpaired electron leading to a nonzero spin density<sup>43</sup>. In contrast, the unpaired electrons do not occur in MoS<sub>2</sub> even if atomic vacancies: S, S<sub>2</sub>, and MoS<sub>3</sub>, are formed, as shown in this study. The reason may be as follows: Mo and S atoms have six and three Mo–S bonds, respectively, and six valence electrons. Thus S atom has three extra valence electrons, not used in the single bonds. For the S, S<sub>2</sub>, and MoS<sub>3</sub> vacancies, three, six and nine electrons remain unpaired, respectively. These unpaired electrons can be coupled with counter electrons by three extra valence electrons of S, which

leads to the spin-unpolarized state. For the electron doping, as described above, the spin density never vanishes and is believed to make an effect on the spin scattering of charge carriers, lowering the mobility. Contrary to MoS<sub>2</sub>, in graphene, the ambipolar spin vanishing under applied  $V_G$  has been demonstrated and discussed to cause an improvement of the charge mobility by a suppression of the spin scattering of charge carriers<sup>25</sup>. That is, the spin species of a vacancy has magnetic dipolar interaction with the spin of a charge carrier, which disturbs the charge transport, while non-magnetic vacancy does not have such interaction with a charge carrier that usually has a spin in semiconductor materials, which preserves the intrinsic mobility. Therefore, the investigations of the spin states of the atomic vacancies extend our knowledge on the mechanism of the high mobility emergence.

MoS<sub>2</sub> thin-film transistors have been fabricated for the studies presented here, and the n-type transistor operation has been confirmed. The operando ESR measurements under electron doping have been performed with the variable  $V_G$  and temperature. Three kinds of signals: Signals A, B and C, have been observed. Signals A and B increase and Signal C decreases with the applied  $V_G$ , respectively. For Signal A, the spin susceptibility is almost independent of temperature, indicating that the origin of this signal can be ascribed to the degenerated conduction electrons. For Signals B and C, the spin susceptibility shows the Curie-like temperature dependence, which means that the origins of these signals can be ascribed to the isolated spins. To further investigate the ESR signal origins, the DFT and GIPAW calculations have been performed for four types of atomic vacancies: S, S<sub>2</sub>, MoS<sub>3</sub>, and MoS<sub>6</sub>, that are most likely to occur in MoS<sub>2</sub>. As a result, only MoS<sub>6</sub> vacancy has a non-vanishing spin density without the electron doping, which enables us to identify Signal C origin to be associated with the MoS<sub>6</sub> vacancy. In order to identify the origin of Signal B, the observed  $g$ -factor has been compared with that from the GIPAW calculations for S, S<sub>2</sub>, and MoS<sub>3</sub> vacancies. As a result, only the  $g$ -factors calculated for the S vacancy agree with the ESR Signal B. Interestingly, the  $g$ -factors of Signals A and B show the temperature dependencies, which we assign to an effect of the SOS in MoS<sub>2</sub> using the Mori–Kawasaki formula. In conclusion, the spin states of the conduction electrons and atomic vacancies (defects), being present in the MoS<sub>2</sub> thin film, have been clarified in this study by the operando ESR measurement during the device operation, to our knowledge for the first time. This result gives a deep insight into our understanding of the spin states in MoS<sub>2</sub> from the microscopic point of view and suggests a combined theoretical and experimental approach for other 2D TMDs. The previous ESR works have mainly studied MoS<sub>2</sub> materials, where the spin states in MoS<sub>2</sub> cannot be electrically controlled. In contrast, the present study reports the electrically controlled spin-state investigations in MoS<sub>2</sub> with the device structure, which is more important to understand the behavior in MoS<sub>2</sub> under device operation compared to the ESR studies of MoS<sub>2</sub> materials without electrically doped charges. This is a novel point of our study compared to the previous ESR studies of MoS<sub>2</sub> materials.

## Methods

**Fabrication of MoS<sub>2</sub> thin film with multi-step CVD method.** A sapphire (Al<sub>2</sub>O<sub>3</sub>) substrate (3 mm × 20 mm) was cleaned by ultrasonic with acetone and 2-propanol and then cleaned by ultraviolet ozone. A MoO<sub>3</sub> (99.9%, Sigma Aldrich) thin film of 3 nm was fabricated on the sapphire substrate with a vacuum deposition method under  $1 \times 10^{-5}$  Pa. To crystallize the MoO<sub>3</sub> film, the film was annealed at 325 °C for 120 min under O<sub>2</sub> atmosphere at 200 sccm (standard cubic centimeter per minute). Sulfur powder was placed on a quartz boat, which was placed side by side with the MoO<sub>3</sub> film in a quartz tube. The sulfur powder and the MoO<sub>3</sub> film were heated at 275 and 550 °C, respectively, under N<sub>2</sub> 50 sccm at atmospheric pressure for 60 min, which sulfurized the MoO<sub>3</sub> film to produce MoS<sub>2</sub>. An annealing treatment was performed at 1000 °C for 30 min under Ar 200 sccm atmosphere to improve the crystallinity. The characterization of the MoS<sub>2</sub> film was performed by measuring

the EDX mapping, cross-sectional TEM image, X-ray diffraction patterns, atomic force microscope image, and Raman spectra, which are presented in Supplementary Figs. 11–15 and Supplementary Table 2, respectively. These data confirm the thickness of 3 nm and the quality of the fabricated MoS<sub>2</sub> film. The fabricated MoS<sub>2</sub> with the 3-nm thickness corresponds to 5 layers with a lattice spacing of 0.62 nm<sup>32,33</sup>.

**Fabrication of transistors with MoS<sub>2</sub>.** Ni/Au (1/49 nm) layers were fabricated as electrodes on the MoS<sub>2</sub> film on the sapphire substrate by a vacuum vapor deposition method with a very slow deposition rate of  $\leq 0.1 \text{ \AA s}^{-1}$  using an ULVAC VPC-260F system. An ion-gel solution was fabricated with ionic liquid 1-ethyl-3-methylimidazolium bis(trifluoromethylsulfonyl)imide ([EMIM][TFSI]) (36 wt%) (Ionic Liquids Technologies, Inc.), an ABA triblock polymer poly(styrene-*b*-methylmethacrylate-*b*-styrene) (3 wt%) (Polymer Source, Inc.), and a solvent ethyl acetate (61 wt%) (Wako Pure Chemical Industries, Ltd.); the solution was stirred for >1 day. The ionic liquid [EMIM][TFSI] has a cation EMIM<sup>+</sup> and an anion TFSI<sup>-</sup>, which electrostatically attract each other. The EMIM<sup>+</sup> and TFSI<sup>-</sup> are nonmagnetic without spin, which do not affect the spin states of the MoS<sub>2</sub> film. The ion-gel layer was formed on an ultrasonically cleaned PET substrate (3 mm × 20 mm) by a drop-cast method, followed by a vacuum annealing treatment at 70 °C for >2 days. The reason for the formation of the ion-gel on the PET substrate is to remove the solvent ethyl acetate without the contact between the solvent and MoS<sub>2</sub> film. The ion-gel insulating layer has an EDL and high ion conductivity<sup>44–46</sup>. The capacitance of the EDL is generally very large, causing a high charge-density state at low voltage and a high on/off ratio in transistor operation. After the vacuum annealing treatment, the ion-gel layer on the PET substrate and the MoS<sub>2</sub> thin film on sapphire substrate were transferred into a glove box (O<sub>2</sub> < 0.2 ppm, H<sub>2</sub>O < 0.5 ppm) and annealed at 70 °C for  $\geq 2$  h to remove the adsorbed moisture. The reason for the use of the Au electrodes is that Au is more stable than other metals under high electric field at the interface with the ion-gel. The issue of the work–function difference can be overcome by the formation of the EDLs at the interface between the Au electrode and ion-gel<sup>44–46</sup>. A wiring was performed using a silver paste in the glove box, and finally the ion-gel layer was laminated on the MoS<sub>2</sub> thin film. The fabricated transistor was placed into an ESR sample tube and sealed in it, where the inside of the sample tube was replaced with a He atmosphere. Supplementary Fig. 16 shows the photographs of the fabrication process of the transistor shown in Fig. 1a, c. We could not observe a clear change of the ESR signals of the MoS<sub>2</sub> film by the electrode deposition, which indicates that the number of deposition-induced defects in the MoS<sub>2</sub> film are negligibly smaller than that of the observed spin species in the MoS<sub>2</sub> film. Thus we have confirmed no impact of device fabrication on our conclusions. The parts of the above-mentioned fabrication method have been described in the previous work<sup>25</sup>.

**Measurements with device analyzer and ESR.** Transfer characteristics were measured with a device analyzer (KEYSIGHT B1500A). The  $V_D$  was fixed at 1 V and the  $V_G$  was swept from 0 to 1.5 V, where the data were measured every 30 mV per 60 s at each point. ESR measurements were performed with a X-band ESR spectrometer (JEOL RESONANCE JES-FA200) equipped with a liquid-He temperature control system (temperature controller and cryostat) (JEOL RESONANCE ES-CT470) and a source meter (Keithley 2612A). The modulation amplitude of the ESR measurements was 0.3 mT.

**Evaluation of spin concentration.** For Signal B, the number of spins ( $N_{\text{spin}}$ ) was evaluated by doubly integrating the difference ESR spectrum at 40 K and comparing it with a Mn<sup>2+</sup> marker. Considering the Curie law and the temperature correction at room temperature (297 K), the  $N_{\text{spin}}$  was evaluated as  $N_{\text{spin}} = 8.84 \times 10^{12}$ . In the same way, the  $N_{\text{spin}}$  of Signal C was evaluated to be  $N_{\text{spin}} = 49.2 \times 10^{12}$ . The used active area of the transistor structure is 0.5 mm × 12 mm = 6.0 mm<sup>2</sup> =  $6.0 \times 10^{-2}$  cm<sup>2</sup>. Since the MoS<sub>2</sub> thin film used in this experiment has five stacked layers, the spin concentration per the MoS<sub>2</sub> unit cell is calculated to be approximately 3 and 16% for Signals B and C, respectively, using the lattice constant of MoS<sub>2</sub> as 3.16 Å.

**DFT calculations.** DFT calculations were performed using the Quantum ESPRESSO package<sup>47</sup>, which is a plane-wave basis tool with the pseudopotentials describing the core electrons. For the  $g$ -tensor calculations, the norm-conserving GIPAW pseudopotentials were used<sup>48,49</sup>, with the energy cut-off 60 Ry. The  $g$ -tensor was obtained with the QE-GIPAW post-processing code<sup>30,50</sup>. The uniform mesh of  $k$ -points was set to 12 × 12 × 1 for the elementary cell, and 9 × 9 × 1 and 6 × 6 × 1 meshes for the 3 × 3 × 1 and 4 × 4 × 1 supercells, respectively. The vacuum separation between the periodic images of the 2D layers was set to 20 Å. We used the supercells of 4 × 4 unit cells for the calculations with the defects. The distance between defects was 12.95 Å, while the chemical definition of the distance at which molecules do not interact is 10 Å. The comparison between the experimentally observed spin density and the defect density of the simulated material or the effect of the supercell size on the calculated results is an interesting issue because we can achieve high charge-density states by the ion-gel in the devices, which is in progress and will be reported in a separate paper.



The band structures were interpolated using the maximally localized Wannier functions<sup>51</sup> implemented in the wannier90 tool<sup>52</sup>. The spin-polarization maps were plotted with the XCrySDen tool<sup>53</sup>.

### Data availability

Data that support the findings of this study are available from the corresponding author upon reasonable request and can also be found at the following persistent repository: <https://figshare.com/s/e08f7108e71b3dc9f631>.

Received: 21 May 2020; Accepted: 3 February 2021;

Published online: 05 March 2021

### References

- Song, I., Park, C. & Choi, H. C. Synthesis and properties of molybdenum disulfide: from bulk to atomic layers. *RSC Adv.* **5**, 7495–7514 (2015).
- Xiao, D. et al. Coupled spin and valley physics in monolayers of MoS<sub>2</sub> and other group-VI dichalcogenides. *Phys. Rev. Lett.* **108**, 196802 (2012).
- Kim, S. et al. High-mobility and low-power thin-film transistors based on multilayer MoS<sub>2</sub> crystals. *Nat. Commun.* **3**, 1011–1017 (2012).
- Wang, Q. H., Kalantar-Zadeh, K., Kis, A., Coleman, J. N. & Strano, M. S. Electronics and optoelectronics of two-dimensional transition metal dichalcogenides. *Nat. Nanotechnol.* **7**, 699–712 (2012).
- Choudhary, N., Patel, M. D., Park, J., Sirota, B. & Choi, W. Synthesis of large scale MoS<sub>2</sub> for electronics and energy applications. *J. Mater. Res.* **31**, 824–831 (2016).
- Kumar, R. et al. A review on synthesis of graphene, h-BN and MoS<sub>2</sub> for energy storage applications: recent progress and perspectives. *Nano Res.* **12**, 2655–2694 (2019).
- Splendiani, A. et al. Emerging photoluminescence in monolayer MoS<sub>2</sub>. *Nano Lett.* **10**, 1271–1275 (2010).
- Radisavljevic, B., Radenovic, A., Brivio, J., Giacometti, V. & Kis, A. Single-layer MoS<sub>2</sub> transistors. *Nat. Nanotechnol.* **6**, 147–150 (2011).
- Ellis, J. K., Lucero, M. J. & Scuseria, G. E. The indirect to direct band gap transition in multilayered MoS<sub>2</sub> as predicted by screened hybrid density functional theory. *Appl. Phys. Lett.* **99**, 261908 (2011).
- Yin, Z. et al. Single-layer MoS<sub>2</sub> phototransistors. *ACS Nano* **6**, 74–80 (2012).
- Ye, J. T. et al. Superconducting dome in a gate-tuned band insulator. *Science* **338**, 1193–1196 (2012).
- Zhang, Y. J., Oka, T., Suzuki, R., Ye, J. T. & Iwasa, Y. Electrically switchable chiral light-emitting transistor. *Science* **344**, 725–729 (2014).
- Zhang, Y. J., Shi, W., Ye, J. T., Suzuki, R. & Iwasa, Y. Robustly protected carrier spin relaxation in electrostatically doped transition-metal dichalcogenides. *Phys. Rev. B* **95**, 205302 (2017).
- Cheiwchanchamnangij, T. & Lambrecht, W. R. L. Quasiparticle band structure calculation of monolayer, bilayer, and bulk MoS<sub>2</sub>. *Phys. Rev. B* **85**, 205302 (2012).
- Roldán, R. et al. Electronic properties of single-layer and multilayer transition metal dichalcogenides MX<sub>2</sub> (M = Mo, W and X = S, Se). *Ann. Phys.* **526**, 347–357 (2014).
- Kormányos, A. et al. k-p theory for two-dimensional transition metal dichalcogenide semiconductors. *2D Mater.* **2**, 022001 (2015).
- Neal, A. T., Liu, H., Gu, J. & Ye, P. D. Magneto-transport in MoS<sub>2</sub>: phase coherence, spin-orbit scattering, and the Hall factor. *ACS Nano* **7**, 7077–7082 (2013).
- Zhou, Y., Yang, P., Zu, H., Gao, F. & Zu, X. Electronic structures and magnetic properties of MoS<sub>2</sub> nanostructures: atomic defects, nanoholes, nanodots and antidots. *Phys. Chem. Chem. Phys.* **15**, 10385–10394 (2013).
- Zheng, H. et al. Tuning magnetism of monolayer MoS<sub>2</sub> by doping vacancy and applying strain. *Appl. Phys. Lett.* **104**, 132403 (2014).
- Houssa, M., Iordanidou, K., Pourtois, G., Afanas'ev, V. V. & Stesmans, A. Point defects in MoS<sub>2</sub>: comparison between first-principles simulations and electron spin resonance experiments. *Appl. Surf. Sci.* **416**, 853–857 (2017).
- Chiappe, D. et al. Controlled sulfurization process for the synthesis of large area MoS<sub>2</sub> films and MoS<sub>2</sub>/WS<sub>2</sub> heterostructures. *Adv. Mater. Interfaces* **3**, 1–10 (2016).
- Marumoto, K., Kuroda, S., Takenobu, T. & Iwasa, Y. Spatial extent of wave functions of gate-induced hole carriers in pentacene field-effect devices as investigated by electron spin resonance. *Phys. Rev. Lett.* **97**, 256603 (2006).
- Nagamori, T. & Marumoto, K. Direct observation of hole accumulation in polymer solar cells during device operation using light-induced electron spin resonance. *Adv. Mater.* **25**, 2362–2367 (2013).
- Sato, G. et al. Direct observation of radical states and the correlation with performance degradation in organic light-emitting diodes during device operation. *Phys. Status Solidi A* **215**, 1700731 (2018).
- Fujita, N. et al. Direct observation of electrically induced Pauli paramagnetism in single-layer graphene using ESR spectroscopy. *Sci. Rep.* **6**, 34966 (2016).
- Stesmans, A. et al. Paramagnetic intrinsic defects in polycrystalline large-area 2D MoS<sub>2</sub> films grown on SiO<sub>2</sub> by Mo sulfurization. *Nanoscale Res. Lett.* **12**, 283 (2017).
- Schoenaers, B., Stesmans, A. & Afanas'ev, V. V. The nitrogen acceptor in 2H-polytype synthetic MoS<sub>2</sub>: frequency and temperature dependent ESR analysis. *Phys. Status Solidi C* **14**, 1700211 (2017).
- Schoenaers, B., Stesmans, A. & Afanas'ev, V. V. Nitrogen acceptor in 2H-polytype synthetic MoS<sub>2</sub> assessed by multifrequency electron spin resonance. *J. Vac. Sci. Technol. A* **36**, 05G503 (2018).
- Stesmans, A., Schoenaers, B. & Afanas'ev, V. V. Variations of paramagnetic defects and dopants in geo-MoS<sub>2</sub> from diverse localities probed by ESR. *J. Chem. Phys.* **152**, 234702 (2020).
- Pickard, C. J. & Mauri, F. First-principles theory of the EPR *g* tensor in solids: defects in quartz. *Phys. Rev. Lett.* **88**, 4 (2002).
- Oshikawa, M. & Affleck, I. Electron spin resonance in *S* = 1/2 antiferromagnetic chains. *Phys. Rev. B* **65**, 134410 (2002).
- Heo, S., Hayakawa, R. & Wakayama, Y. Carrier transport properties of MoS<sub>2</sub> field-effect transistors produced by multi-step chemical vapor deposition method. *J. Appl. Phys.* **121**, 024301 (2017).
- Jeong, Y. et al. Structural characterization and transistor properties of thickness-controllable MoS<sub>2</sub> thin films. *J. Mater. Sci.* **54**, 7758–7767 (2019).
- Lee, J. et al. Ion gel-gated polymer thin-film transistors: operating mechanism and characterization of gate dielectric capacitance, switching speed, and stability. *J. Phys. Chem. C* **113**, 8972–8981 (2009).
- Pearce, A. J. & Burkard, G. Electron spin relaxation in a transition-metal dichalcogenide quantum dot. *2D Mater.* **4**, 025114 (2017).
- Kormányos, A., Zolyomi, V., Drummond, N. D. & Burkard, G. Spin-orbit coupling, quantum dots, and qubits in monolayer transition metal dichalcogenides. *Phys. Rev. X* **4**, 011034 (2014).
- Žutić, I., Fabian, J. & Das Sarma, S. Spintronics: fundamentals and applications. *Rev. Mod. Phys.* **76**, 323–410 (2004).
- Mori, H. & Kawasaki, K. Theory of dynamical behaviors of ferromagnetic spins. *Prog. Theor. Phys.* **27**, 529–570 (1962).
- Zhou, W. et al. Intrinsic structural defects in monolayer molybdenum disulfide. *Nano Lett.* **13**, 2615–2622 (2013).
- Schoenaers, B. et al. Analysis of transferred MoS<sub>2</sub> layers grown by MOCVD: evidence of Mo vacancy related defect formation. *ECS J. Solid State Sci. Technol.* **9**, 093001 (2020).
- Hwang, E. H., Adam, S. & Das Sarma, S. Carrier transport in two-dimensional graphene layers. *Phys. Rev. Lett.* **98**, 186806 (2007).
- Lembke, D., Bertolazzi, S. & Kis, A. Single-layer MoS<sub>2</sub> electronics. *Acc. Chem. Res.* **48**, 100–110 (2015).
- Ma, Y., Lehtinen, P. O., Foster, A. S. & Nieminen, R. M. Magnetic properties of vacancies in graphene and single-walled carbon nanotubes. *New J. Phys.* **6**, 68 (2004).
- Panzer, M. J. & Frisbie, C. D. Exploiting ionic coupling in electronic devices: electrolyte-gated organic field-effect transistors. *Adv. Mater.* **20**, 3176–3180 (2008).
- Cho, J. H. et al. Printable ion-gel gate dielectrics for low-voltage polymer thin-film transistors on plastic. *Nat. Mater.* **7**, 900–906 (2008).
- Pu, J. et al. Highly flexible MoS<sub>2</sub> thin-film transistors with ion gel dielectrics. *Nano Lett.* **12**, 4013–4017 (2012).
- Giannozzi, P. et al. QUANTUM ESPRESSO: a modular and open-source software project for quantum simulations of materials. *J. Phys. Condens. Matter* **21**, 395502 (2009).
- Pickard, C. J. & Mauri, F. All-electron magnetic response with pseudopotentials: NMR chemical shifts. *Phys. Rev. B* **63**, 245101 (2001).
- Blöchl, P. E. Projector augmented-wave method. *Phys. Rev. B* **50**, 17953–17979 (1994).
- Pickard, C. J. & Mauri, F. Nonlocal pseudopotentials and magnetic fields. *Phys. Rev. Lett.* **91**, 196401 (2003).
- Marzari, N., Mostofi, A. A., Yates, J. R., Souza, I. & Vanderbilt, D. Maximally localized Wannier functions: theory and applications. *Rev. Mod. Phys.* **84**, 1419–1475 (2012).
- Pizzi, G. et al. Wannier90 as a community code: new features and applications. *J. Phys. Condens. Matter* **32**, 165902 (2020).
- Kokalj, A. Computer graphics and graphical user interfaces as tools in simulations of matter at the atomic scale. *Comput. Mater. Sci.* **28**, 155–168 (2003).

### Acknowledgements

DFT calculations were performed in the Cyfronet Computer Centre using the Prometheus computer. This work was partially supported by JSPS KAKENHI Grant Numbers JP19K21955 and JP19K05201, by JST PRESTO, by The Hitachi Global

Foundation, by The MIKIYA Science and Technology Foundation, by The Futaba Foundation, and by JST ALCA Grant Number JPMJAL1603, Japan.

### Author contributions

N.T. and K.M. conceived and designed this work. N.T., S.I., Y.Won, and K.M. fabricated all the devices, performed the experiments, and analyzed the data. M.W. performed the DFT calculations of  $g$ -factor and spin-density distribution. A.U. performed the calculation of the effective  $g$ -factor at finite temperature. N.T., S.H., Y.J., and Y.Wakayama fabricated all MoS<sub>2</sub> thin films. N.T., M.W., A.U., and K.M. wrote the manuscript. K.M. supervised this work. All authors discussed the results and reviewed the manuscript.

### Competing interests

The authors declare no competing interests.

### Additional information

**Supplementary information** The online version contains supplementary material available at <https://doi.org/10.1038/s43246-021-00129-y>.

**Correspondence** and requests for materials should be addressed to K.M.

**Peer review information** Primary handling editor: Aldo Isidori

**Reprints and permission information** is available at <http://www.nature.com/reprints>

**Publisher's note** Springer Nature remains neutral with regard to jurisdictional claims in published maps and institutional affiliations.



**Open Access** This article is licensed under a Creative Commons Attribution 4.0 International License, which permits use, sharing, adaptation, distribution and reproduction in any medium or format, as long as you give appropriate credit to the original author(s) and the source, provide a link to the Creative Commons license, and indicate if changes were made. The images or other third party material in this article are included in the article's Creative Commons license, unless indicated otherwise in a credit line to the material. If material is not included in the article's Creative Commons license and your intended use is not permitted by statutory regulation or exceeds the permitted use, you will need to obtain permission directly from the copyright holder. To view a copy of this license, visit <http://creativecommons.org/licenses/by/4.0/>.

© The Author(s) 2021